PAPER

Mn^{4+}-activated oxyfluoride K$_3$TaOF$_6$ red phosphor with intense zero phonon line for warm white light-emitting diodes†

Jiao Wu, Bo Wang, [ID]* Zhiyuan Liu, Kang Zhang and Qingguang Zeng*

The intense zero phonon line (ZPL) of the Mn^{4+}:^{2}E→^{4}A$_2$ transition can further promote the color rendering and luminous efficiency for high-quality white-emitting diodes (w-LEDs). In this article, a Mn^{4+}-activated K$_3$TaOF$_6$ oxyfluoride red phosphor was synthesized *via* a facile two-step method. Its phase and morphology were characterized by X-ray diffraction, SEM and TEM. The as-prepared K$_3$TaOF$_6$:Mn^{4+} exhibits an intense absorption of blue light and a strong emission band peaking at 628 nm with a color purity as high as 96.4%. Attributed to the distorted octahedral coordination environment of Mn^{4+} ions, an intense ZPL emission was detected at 620 nm. By theoretical calculation, Mn^{4+} ions in the K$_3$TaOF$_6$ host experience a strong crystal field. In addition, the temperature-dependent PL and thermoluminescence (TL) spectra suggest that thermal ionization dominates the thermal quenching phenomenon in this phosphor.

1. Introduction

With the development of lighting and display technology in the past decades, there is an increasing requirement of the color quality of white lighting-emitting diode (w-LED) illuminant sources.[1–5] However, the commercially available w-LED devices, *i.e.*, based on Y$_3$Al$_5$O$_{12}$:Ce^{3+} (YAG) yellow phosphors with InGaN blue chips are unsuitable for liquid crystal display (LCD) backlights due to their limited color gamut.[6–8] As an alternative, combining commercial CaAlSiN$_3$:Eu^{2+} red phosphors with β-sialon:Eu^{2+} green phosphors has been a popular model in the LCD backlight market.[9,10] Unfortunately, the excitation band of CaAlSiN$_3$:Eu^{2+} is so broad that serious re-absorption between β-sialon:Eu^{2+} and CaAlSiN$_3$:Eu^{2+} will be caused, which then brings the change of color and a reduction of luminous efficacy.[11] Moreover, the LCD backlight obtained *via* this approach can only reach ∼82% of the required standard proposed by National Television Standards Committee (NTSC). Conceivably, it is crucial to develop phosphors with appropriate peak position, narrow emission band, high quantum efficiency (QE) and excellent thermal stability to fulfil the application.

Thanks to the specific electronic structure of the Mn^{4+} (3d^3 electron configuration) ion, obvious broadening of the color gamut of LED-lit LCD backlights has been observed by employing Mn^{4+}-activated red phosphors.[12–18] Theoretically, both Stokes and anti-Stokes photon vibrational sidebands could

be easily implemented in the transition of Mn^{4+}:^{2}E→^{4}A$_2$.[16,17] Whereas, only when Mn^{4+} ions have distorted coordination geometries can the ZPL transition of Mn^{4+}:^{2}E→^{4}A$_2$ occur.[19–22] Generally, the sharpest PL emission of the Mn^{4+} ion is located at ∼630 nm among a group of sharp emission peaks while the observed ZPL emission in a few cases peaks at ∼620 nm.[8,21,22] In fact, as part of the PL emission, the ZPL emission is of great benefit to improve the luminous efficiency because human eyes are more sensitive to shorter wavelengths.[8,12,14] In spite of the absence of distorted octahedral coordination sites, the oxyfluoride compounds still can provide distorted local environments by F/O mixed-ligands, which could bring rich spectroscopic properties, thus many researchers have focused on the oxyfluoride compounds.[22] For instance, new fluorotungstate red-emitting phosphors A$_2$WO$_2$F$_4$:Mn^{4+} (A = Na, Cs) were successfully synthesized through a co-precipitation method and intense ZPL emissions were detected under blue light excitation.[22,23] Similarly, in the newly obtained fluoromolybdate red phosphor Cs$_2$MoO$_2$F$_4$:Mn^{4+}, the ZPL emission is also observed despite the lower intensity compared with the phonon sidebands.[24]

In this work, a fluorotantalate compound, *i.e.*, K$_3$TaOF$_6$ which can offer a distorted octahedral polyhedron was taken as the matrix. The host material was synthesized by the solid-state reaction and samples of K$_3$TaOF$_6$:Mn^{4+} were prepared through the hydrothermal method. The high phase purity of the as-prepared samples was demonstrated by XRD and TEM analyses. As expected, an intense ZPL at 620 nm was observed in K$_3$TaOF$_6$:Mn^{4+} upon blue light excitation. In this article, the synthetic method, luminescence property and thermal quenching of this series of phosphors will be reported.

School of Applied Physics and Materials, Wuyi University, Jiangmen, Guangdong 529020, P. R. China. E-mail: wangbo312@mails.ucas.ac.cn; zengqg@mail.ustc.edu.cn

† Electronic supplementary information (ESI) available. See DOI: 10.1039/d1ra05174a

2. Sample preparation

The raw materials used for the synthesis were Ta_2O_5 (A.R.), KF (A.R.), K_2TaF_7 (A.R.), $KMnO_4$ (99.99%), KHF_2 (A.R.), HF (49%) and H_2O_2 (30%).

The Mn^{4+}-activated fluorotantalate K_3TaOF_6:Mn^{4+} phosphor was prepared *via* the solid-state reaction and hydrothermal method in sequence (Fig. 1(a)).

Step I: pure K_3TaOF_6 host powder was synthesized by the following stoichiometric equation:[25]

$$3K_2TaF_7 + Ta_2O_5 + 9KF \rightarrow 5K_3TaOF_6 \qquad (1)$$
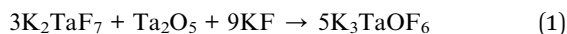
The mixtures were heated at 900 °C for 0.5 h under an Ar atmosphere. As presented in Fig. 1(b), the main XRD diffraction peaks of the as-obtained host are consistent with the standard XRD pattern of K_3TaOF_6 (PDF No. 29-1052). Then powders of the obtained K_3TaOF_6 and prefabricated K_2MnF_6 in different molar ratios were mixed and ground for 0.5 h in an agate mortar. K_2MnF_6 was obtained from previous work.[19]

Step II: loaded the mixtures into Teflon-lined autoclaves and added a drizzle of HF. The autoclaves were heated to 180 °C, kept for 1 h, and then cooled down to room temperature. Finally, the product was collected by centrifugation, subsequently washed with ethanol for three times and dried at 120 °C for 8 h.

The obtained diffraction peaks of K_3TaOF_6:Mn^{4+} also agree well with the standard data of K_3TaOF_6 and no impurity phase was observed with the increasing doping amount of K_2MnF_6,

illustrating the high phase purity of the as-obtained K_3TaOF_6:Mn^{4+} samples.

3. Results and discussion

3.1 Phase, morphology and composition

Fig. 2(a) shows the XRD Rietveld refinement results of K_3TaOF_6:$0.04Mn^{4+}$. The experimental data are consistent with calculated patterns deriving from the K_3NbOF_6 matrix (ICSD code: 26634). The good weight-and profile-R-parameters (R_p = 5.94% and R_{wp} = 8.56%) prove the high match of K_3TaOF_6 to K_3NbOF_6. Then, the cell volumes for K_3TaOF_6:xMn^{4+} as determined by Rietveld refinement of powder XRD data is presented in Fig. S1.† According to the results, the volumes gradually decrease with the change of x from 0 to 0.12, due to the Ta^{5+} and Mn^{4+} ions have the different radius. In the structure of K_3TaOF_6, each Ta atom may be coordinated by six F atoms and one O atom and form a highly disordered octahedron of $[TaOF_6]^{3-}$. Once the Mn^{4+} ions invade the crystal lattice of K_3TaOF_6, the similar ionic radii between Mn^{4+} and Ta^{5+} ions make Mn^{4+} ions easy to occupy the sites of Ta^{5+} ions. However, the substitution of Mn^{4+} ions for Ta^{5+} ions would inevitably bring some point defects. The doped phase can be represented through the formula $K_3Ta_{(1-x)}Mn_xO_{(1-y)}(Vox)_yF_6$, with oxygen vacancies (Vox) in the lattice (alternately F vacancies). Meanwhile, Ta^{5+}

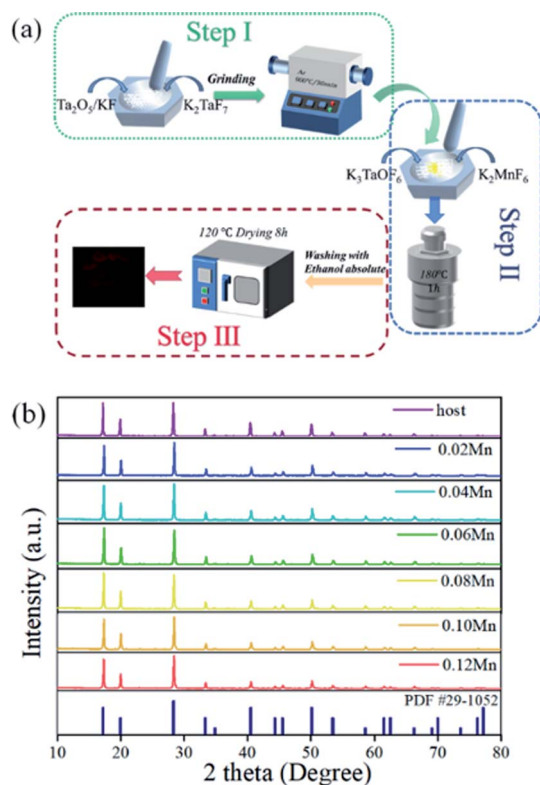**Fig. 1** (a) Synthesis schematic diagram of K_3TaOF_6 and K_3TaOF_6:Mn^{4+} (b) X-ray diffraction patterns of K_3TaOF_6:Mn^{4+} samples.
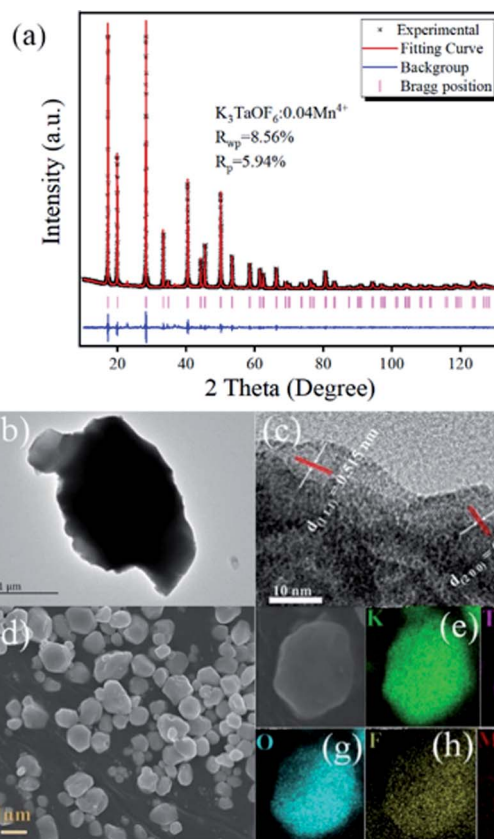

Fig. 2 (a) Rietveld refinements of the observed XRD patterns for the K_3TaOF_6:$0.04Mn^{4+}$. (b) and (c) TEM and HRTEM diagram of the K_3TaOF_6:$0.04Mn^{4+}$. (d)–(i) SEM image of K_3TaOF_6:$0.04Mn^{4+}$ and EDS mapping images of K, Ta, O, F and Mn elements.

and Mn^{4+} cations would coexist which would require electrical compensation with O or F vacancies. The highly-distorted octahedral coordination environment of Mn^{4+} ions may induce the local symmetry to lose the inversion centre, which is expected to heighten the emission intensity of ZPL, while the crystal defects would has serious effect for the thermal stability.[26]

TEM analysis in Fig. 2(b) demonstrates that the whole particle of the K_3TaOF_6:0.04Mn^{4+} sample exhibits the crystalline nature. Moreover, with the help of HRTEM, lattice fringes could be observed clearly in Fig. 2(c) and two interplanar spacings of 5.15 Å and 4.45 Å were obtained, which are corresponding to the (1 1 1) and (2 0 0) plane of K_3TaOF_6, respectively. From Fig. 2(d), it can be seen that the represented particles of K_3TaOF_6:0.04-Mn^{4+} have irregular morphology with the size of particle being ~3 μm and exhibit a degree of particle agglomeration. Moreover, the energy dispersive X-ray spectroscopy (EDS) elemental mapping technique was used to confirm the composition uniformity of K_3TaOF_6:Mn^{4+}, as presented in Fig. 2(e)–(i). The elemental mapping images exhibit that K, Ta, O, F and Mn are homogeneously distributed within the phosphor particle. In addition, the atom percentages of K, Ta, O, F element are 26.2%, 10.3%, 11.5% and 52.0%, respectively, which is close to $3 : 1 : 1 : 5$ of K_3TaOF_6.

3.2 Room-temperature photoluminescence

Fig. S2(a)† shows the diffuse reflection spectrum (DRS) of K_3TaOF_6:$x$$Mn^{4+}$ phosphors. The absorption in the blue and UV region arises from the spin-allowed transition of the Mn^{4+} ion in d^3 configuration. Based on the DR spectrum of non-doped sample, the optical band gap (E_{gap}) of the K_3TaOF_6 host calculated from the Kubelka–Munk's equations[27] is approximately 4.04 eV, as denoted in Fig. S2(b).† When the Mn^{4+} ions are embedded into the host lattice, some well-localized energy states belonging to the ground configuration and excited configuration of impurity are introduced between the valence and the conduction bands of the host. Such a wide band gap could provide enough space to accommodate the energy levels of the activator, which can restrain the overlap between the excited state and conduction band.

Fig. 3(a) displays the 3D PL emission spectra of K_3TaOF_6:0.04Mn^{4+} with different excitation wavelengths at room temperature. Under various photon irradiation, the shape and position of characteristic peaks almost unchanged, indicating the good color stability of K_3TaOF_6:0.04Mn^{4+}. Then, iso-intensity contours at the longer excitation wavelengths were recorded to typical 2D photoluminescence excitation (PLE) and PL spectra (Fig. 3(b) and (c)) for further analysis. The emission spectrum excited by 470 nm blue light shows spin-forbidden $^2E_g \rightarrow ^4A_{2g}$ transition peaks with phonon-coupled vibronic Stokes/anti-Stokes modes of $MnOF_6$ octahedron. Obviously, an intense ZPL was recorded at about 620 nm, credited to the extremely distorted coordination environment of Mn^{4+} ions. The PLE spectrum detecting at 628 nm shows two wide excitation bands at 470 nm and 370 nm, assigned to the spin-allowed $^4A_{2g} \rightarrow ^4T_{2g}$ and $^4A_{2g} \rightarrow ^4T_{1g}$ transitions of Mn^{4+} ions,
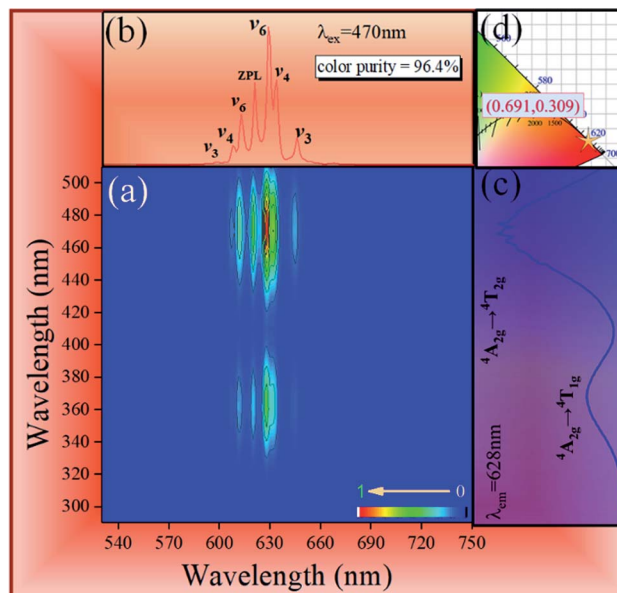

Fig. 3 (a) The contour plots for the PL emission spectra of K_3-$TaOF_6$:0.04Mn^{4+} with various excitation wavelength. (b) and (c) The sliced spectra for excitation and emission bands. (d) CIE coordinates of the light emitted by the sample.

respectively.[19,20] Notably, a substantial overlap between the broad blue absorption band and the emission region of InGaN blue chip were found, indicating that K_3TaOF_6:0.04Mn^{4+} could be a promising candidate for LCD. Moreover, the obtained CIE chromaticity coordinates of (0.691, 0.309) calculated from the emission spectrum are quite close to the red color standard values of (0.67, 0.33) and the correlated color temperature calculated to be 4451 K, as shown in Fig. 3(d).[28] Besides, the color purity of this red phosphor was evaluated to be 96.4%, attributing to its narrow emission band.[29] Consequently, K_3TaOF_6:0.04Mn^{4+} is a promising red phosphor which has potential application in backlit display field. To achieve the optimization of the luminescence performance of K_3TaOF_6:Mn^{4+}, a group of samples with various molecular concentration of Mn^{4+} ions from 0.02 to 0.12 were synthesized. As displayed in Fig. S3(a),† under the 470 nm blue-light excitation, the integrated intensity exhibits an increase first and the optimal doping concentration of Mn^{4+} ions is 4 mol%, then concentration quenching occurs. It is accepted that non-radiative energy transfer between the adjoining luminescence centers contributed to this phenomenon. Fig. S3(b)† shows the luminescent decay curves of K_3TaOF_6:$x$$Mn^{4+}$ measured under excitation at 470 nm. Evidently, the luminescence of Mn^{4+} ions decays exponentially in K_3TaOF_6 host and the calculated lifetime of this group of samples declines from 4.38 to 3.31 ms with the increase of the concentration. It is believed that the gradually enhanced nonradiative transition between Mn^{4+} ions is responsible for the shortening of the lifetime. Specifically, a lifetime less than 5 ms could efficiently avoid the image-retention phenomenon in the application of backlight display.

The influence of crystal field strength on the energy levels of Mn^{4+} in K_3TaOF_6 could be analyzed via the Tanabe–Sugano diagram. According to Tanabe–Sugano diagram,[17] the values of
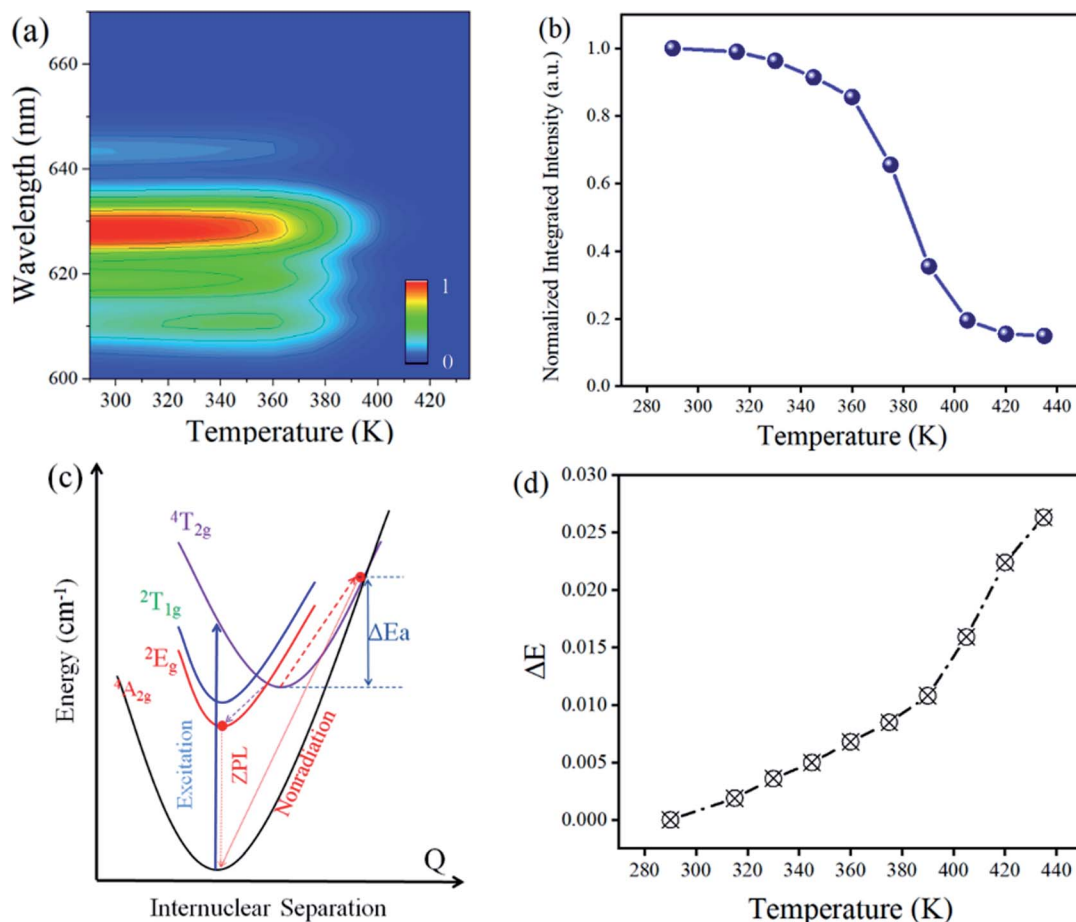
Fig. 4   (a) and (b) Temperature-dependent emission intensity and the corresponding integrated emission intensity of K_3TaOF_6:0.04Mn^{4+}. (c) Configurational coordination diagram for Mn^{4+} in K_3TaOF_6. (d) CIE shift of K_3TaOF_6:0.04Mn^{4+} with various temperature.

the crystal field strength D_q and the Racah parameters B and C of K_3TaOF_6:Mn^{4+} phosphor were calculated to be ~2127 cm^{-1}, 527 cm^{-1} and 3932 cm^{-1}, respectively. Thus, the D_q/B is equivalent to 4.03, implying a high crystal field strength in K_3TaOF_6 host lattice (Fig. S4(a)†).

The nephelauxetic effect caused by the chemical bonds between Mn^{4+} and F^-/O^{2-} ligand often determines the emission energy of Mn^{4+}:$^2E \rightarrow {}^4A_{2g}$. Therefore, a parameter β_1 was adopted to quantitatively describe the nephelauxetic effect in the spectroscopy of the Mn^{4+}:[22]

$$\beta_1 = \sqrt{\left(\frac{B}{B_0}\right)^2 + \left(\frac{C}{C_0}\right)^2} \qquad (2)$$

where the free ion values of B_0 and C_0 of the Mn^{4+} ion are 1160 cm^{-1} and 4303 cm^{-1}, respectively. The value of β_1 for Mn^{4+} in K_3TaOF_6 is then calculated to be 1.02. Notably, the data point followed the empirical line well, as shown in Fig. S4(b).†

3.3   Temperature-dependent luminescence

To get a better study on temperature-dependent luminescence behavior of K_3TaOF_6:Mn^{4+}, the PL spectra of K_3TaOF_6:0.04Mn^{4+} phosphor excited by 470 nm blue light at various temperature (290–435 K) were measured. The temperature-dependent

emission intensity spectra and the corresponding intensity trend were plotted in Fig. 4(a) and (b). Clearly, the integrated PL intensity of K_3TaOF_6:0.04Mn^{4+} decreases with the increasing of temperature and the red phosphor shows a remarkable thermal quenching because of the severer non-radiative transition at higher temperature. The thermal activation energy (ΔE_a) can be determined by Arrhenius equation:[22]

$$I_T = \frac{I_0}{1 + C \times \exp\left(-\dfrac{\Delta E_a}{kT}\right)} \qquad (3)$$

where I_0 is the emission intensity at temperature 290 K, C and k is constant. So the calculated ΔE_a can be determined to be 0.218 eV. With the increasing of temperature, most electrons at $^4T_{2g}$ state will absorb the heat and climb to the crossover point of the $^4T_{2g}$ and $^4A_{2g}$ states once the accumulated energy exceeds ΔE_a. Then, these electrons will return to the ground state $^4A_{2g}$ by a non-radiative way and give rise to thermal quenching, as demonstrated in configurational coordinate diagram (Fig. 4(c))

Besides, color stability is another critical parameter for phosphors, which can be described with CIE shift (ΔE). The calculated equation is as follows:[30,31]
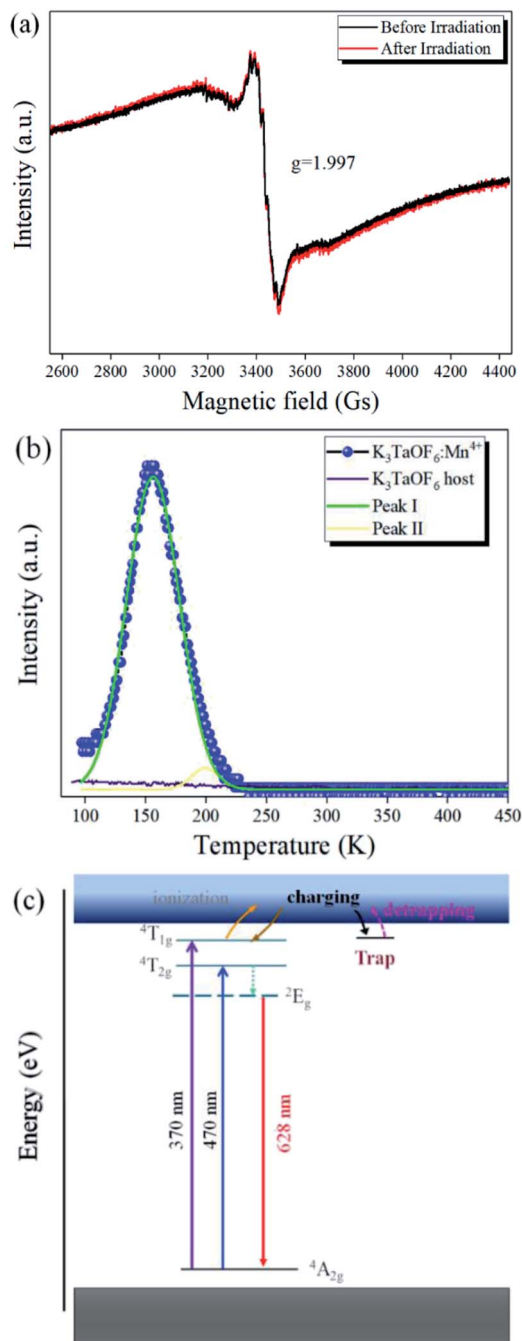
Fig. 5 (a) The EPR spectra of K_3TaOF_6:Mn^{4+} before/after irrational. (b) TL spectrum and theoretically fitted spectra of K_3TaOF_6:Mn^{4+} sample. (c) Schematic illustration of thermal quenching.

$$\Delta E = \sqrt{(u_t - u_0)^2 + (v_t - v_0)^2 + (w_t - w_0)^2} \qquad (4)$$

where $u = 4x/(3 - 2x + 12y)$, $v = 9y/(3 - 2x + 12y)$ and $w = 1 - u - v$. u and v are the chromaticity coordinates in uv uniform color space. As shown in Fig. 4(d), the low ΔE of K_3TaOF_6:Mn^{4+} red phosphor further proves its high color stability and the potential for display devices.

Killer centers would be formed when the Mn^{4+} ions occupy the sites of Ta^{5+} ions, which may accelerate the thermal quenching process. In K_3TaOF_6:Mn^{4+}, there are two kinds of killer centers, such as O or F vacancies. To further study the nature of the traps, EPR was adopted to probe the point defects and impurity ions. As shown in Fig. 5(a), the EPR spectra of the K_3TaOF_6:$0.04Mn^{4+}$ before/after irradiation were recorded. When the specimen was illuminated with blue-light (450 nm), an almost symmetric EPR signal appeared at $g = 1.998$. The negative g shift is attributed to electrons trapped in K_3TaOF_6 host.[32–34] In addition to EPR analysis, to study the thermal ionization process in K_3TaOF_6:$0.04Mn^{4+}$, the thermoluminescence (TL) spectrum monitored by temperature (90–450 K) was collected with the sample exposure to UV light for 120 s, as shown in Fig. 5(b). Obviously, there is one broad band locating at 100–250 K, corresponding to the trapping energy level. Generally, shallow traps are easier to capture and release the electrons or holes than the deep ones. As a consequence, when the temperature reaches to a certain value, the captured electrons or holes would escape from the shallow traps, which leads to thermal quenching. In Fig. 5(b), there are two Gaussian peaks locating at around 156 K and 200 K respectively for K_3TaOF_6:$0.04Mn^{4+}$. The phenomenon that the integrated PL intensity is sensitive to the heating temperature and decreases dramatically with the increasing temperature strongly indicates that thermal ionization is the real villain for thermal quenching of K_3TaOF_6:$0.04Mn^{4+}$. The trap depth E was estimated to range from 0.31 to 0.40 eV according to the equation of $E = T_m/500$, where T_m is the peak temperature. To get a better understand of the process, the charging for TL measurement and thermal quenching induced by thermal ionization was illustrated in Fig. 5(c).

4. Conclusions

In summary, Mn^{4+}-activated fluorotantalate red phosphor K_3TaOF_6 was successfully obtained. This phosphor shows intense red emission peaking at 628 nm along with a high intensity ZPL emission under blue light excitation. The optimal doping concentration of Mn^{4+} ions is 4 mol%. By conducting the TL and EPR analysis, thermal ionization may play a dominant role in the thermal quenching.

Conflicts of interest

The authors declared that they have no conflicts of interest to this work. We declare that we do not have any commercial or associative interest that represents a conflict of interest in connection with the work submitted.

Acknowledgements

2020JC01012, 2020JC01018), the research and development fund of Wuyi university joint Hong Kong-Macao (No. 2019WGALH04, No. 2019WGALH09).

References

1 C. C. Lin and R. S. Liu, Advances in phosphors for light-emitting Diodes, *Phys. Chem. Lett.*, 2011, **2**, 1268–1277.

2 H. A. Höppe, Recent developments in the field of inorganic phosphors, *Angew. Chem., Int. Ed.*, 2009, **48**, 3572–3582.

3 S. Ye, F. Xiao, Y. X. Pan, Y. Y. Ma and Q. Y. Zhang, Phosphors in phosphor-converted white light-emitting diodes recent advances in materials, techniques and properties, *Mater. Sci. Eng., R*, 2010, **71**, 1–34.

4 G. C. Adhikari, H. Y. Zhu, P. A. Vargas and P. F. Zhu, UV-green emission from organolead bromide perovskite nanocrystals, *J. Phys. Chem. C*, 2018, **122**, 15041–15046.

5 G. C. Adhikari, S. Thapa, Y. Yue, H. Y. Zhu and P. F. Zhu, Thiocyanate based all-inorganic perovskite and their applications in white light-emitting diodes, *Photonics*, 2021, **8**, 209.

6 H. X. Liao, Z. Zhao, Y. Y. Zhou, M. S. Molokeev, Q. L. Liu, Q. Y. Zhang and Z. G. Xia, Polyhedron transformation toward stable narrow-band green phosphors for wide-color gamut liquid crystal display, *Adv. Funct. Mater.*, 2019, **29**, 1901988.

7 E. H. Song, Y. Y. Zhou, Y. Wei, X. X. Han, Z. R. Tao, R. L. Qiu, Z. G. Xia and Q. Y. Zhang, A thermally stable narrow-band green-emitting phosphor $MgAl_2O_4$:Mn^{2+} for wide color gamut backlight display application, *J. Mater. Chem. C*, 2019, **7**, 8192–8198.

8 H. Lin, T. Hu, Q. M. Huangn, Y. Cheng, B. Wang, J. Xu, J. M. Wang and Y. S. Wang, Non-rare-earth K_2XF_7:Mn^{4+} (X = Ta, Nb): a highly-efficient narrow-band red phosphor enabling the application in wide-color-gamut LCD, *Laser Photonics Rev.*, 2017, **11**, 1700148.

9 L. Wang, X. J. Wang, T. Kohsei, K. I. Yoshimura, M. Izumi, N. Hirosaki and R. J. Xie, Highly efficient narrow-band green and red phosphors enabling wider color-gamut LED backlight for more brilliant displays, *Opt. Express*, 2015, **23**, 28707–28717.

10 S. X. Li, L. Wang, D. M. Tang, Y. J. Cho, X. J. Liu, X. T. Zhou, L. Lu, L. Zhang, T. Takeda, N. Hirosaki and R. J. Xie, Achieving high quantum efficiency narrow-band β-Sialon:Eu^{2+} phosphors for high-brightness LCD backlights by reducing the Eu^{3+} luminescence killer, *Chem. Mater.*, 2018, **30**, 494–505.

11 B. Wang, H. Lin, J. Xu, H. Chen and Y. S. Wang, $CaMg_2Al_{16}O_{27}$:Mn^{4+}-based red phosphor: a potential color converter for high-powered warm W-LED, *ACS Appl. Mater. Interfaces*, 2014, **6**, 22905–22913.

12 S. G. He, L. Q. Yao, W. T. Cai, D. Wu, J. Q. Peng and X. Y. Ye, A novel Mn^{4+} doped oxyfluoride red phosphor for rapid-response backlights display, *Dalton Trans.*, 2020, **49**, 11290–11299.

13 Q. Y. Wu, C. X. Liao, J. Q. Pan, X. Y. Ye, W. X. You and L. B. Xia, HF-free molten salt route for synthesis of highly efficient and water-resistant K_2SiF_6:Mn^{4+} for warm white LED, *J. Am. Ceram. Soc.*, 2020, **103**, 6901–6912.

14 H. Ming, L. L. Liu, S. A. He, J. Q. Peng, F. Du, J. X. Fu, F. L. Yang and X. Y. Ye, An ultra-high yield of spherical K_2NaScF_6:Mn^{4+} red phosphor and its application in ultra-wide color gamut liquid crystal displays, *J. Mater. Chem. C*, 2019, **7**, 7237–7248.

15 L. Huang, Y. W. Zhu, X. J. Zhang, R. Zou, F. J. Pan, J. Wang and M. M. Wu, HF-Free hydrothermal route for synthesis of highly efficient narrow-band red emitting phosphor $K_2Si_{1-x}F_6$:xMn^{4+} for warm white Light-Emitting Diodes, *Chem. Mater.*, 2016, **28**, 1495–1502.

16 D. Q. Chen, Y. Zhou, W. Xu, J. S. Zhong, Z. G. Ji and W. D. Xiang, Enhanced luminescence of $Y_3Al_5O_{12}$:Mn^{4+} red phosphor via impurity doping, *J. Mater. Chem. C*, 2016, **4**, 1704–1712.

17 B. Wang, H. Lin, F. Huang, J. Xu, H. Chen, Z. B. Lin and Y. S. Wang, Non-rare-earth $BaMgAl_{10-2x}O_{17}$:xMn^{4+},xMg^{2+}: a narrow-band red phosphor for use as a high-power warm w-LED, *Chem. Mater.*, 2016, **28**, 3515–3524.

18 H. Chen, H. Lin, Q. M. Huang, F. Huang, J. Xu, B. Wang, Z. B. Lin, J. C. Zhou and Y. S. Wang, A novel double-perovskite Gd_2ZnTiO_6:Mn^{4+} red phosphor for UV-based w-LEDs: structure and luminescence properties, *J. Mater. Chem. C*, 2016, **4**, 2374–2381.

19 Y. Jin, M. H. Fang, M. Griberg, S. Mahlik, T. Lesniewski, M. G. Brik, G. Y. Luo, J. G. Lin and R. S. Liu, Narrow red emission band fluoride phosphor $KNaSiF_6$:Mn^{4+} for warm white light-emitting diodes, *ACS Appl. Mater. Interfaces*, 2016, **8**, 11194–11203.

20 A. M. Srivatava and W. W. Beers, Luminescence of Mn^{4+} in the distorted perovskite Gd_2MgTiO_6, *J. Electrochem. Soc.*, 1996, **143**, L203–L205.

21 D. Q. Chen, Y. Zhou and J. S. Zhong, A review on Mn^{4+} activators in solids for warm white light-emitting diodes, *RSC Adv.*, 2016, **6**, 86285–86296.

22 T. Hu, H. Lin, Y. Cheng, Q. M. Huang, J. Xu, Y. Gao, J. M. Wang and Y. S. Wang, A highly-distorted octahedron with a C_{2v} group symmetry inducing an ultra-intense zero phonon line in Mn^{4+}-activated oxyfluoride $Na_2WO_2F_4$, *J. Mater. Chem. C*, 2017, **5**, 10524–10532.

23 S. Adachi, Photoluminescence spectra and modeling analyses of Mn^{4+}-activated fluoride phosphors: a review, *J. Lumin.*, 2018, **197**, 119–130.

24 P. Cai, L. Qin, C. Chen, J. Wang and H. J. Seo, Luminescence, energy transfer and optical thermometry of a narrow red emitting phosphor: $Cs_2WO_2F_4$:Mn^{4+}, *Dalton Trans.*, 2017, **46**, 14331–14340.

25 L. Kosa and I. Mackova, Determination of the enthalpy of fusion of K_3TaF_8 and K_3TaOF_6, *Thermochim. Acta*, 2006, **447**, 209–211.

26 S. G. He, F. F. Xu, T. T. Han, Z. Q. Lu, W. Wang, J. Q. Peng, F. Du, F. L. Yang and X. Y. Ye, A Mn^{4+}-doped oxyfluoride phosphor with remarkable negative thermal quenching and high color stability for warm WLEDs, *Chem. Eng. J.*, 2020, **392**, 123657.

27 B. Wang, H. W. Wang, J. H. Huang, J. C. Zhou and P. F. Liu, Trap distribution and photo-stimulated luminescence in LaSrAl$_3$O$_7$:Eu^{2+} long-lasting phosphors for optical data storage, *J. Am. Ceram. Soc.*, 2020, **103**, 315–323.

28 G. C. Adhikari, P. A. Vargas, H. Y. Zhu, A. Grigoriev and P. F. Zhu, Tetradic phosphor white light with variable CCT and superlative CRI through organolead halide perovskite nanocrystals, *Nanoscale Adv.*, 2019, **1**, 1791–1798.

29 Y. Zhou, S. Zhang, X. M. Wang and H. Jiao, Structure and luminescence properties of Mn^{4+}-activated K$_3$TaO$_2$F$_4$ red phosphor for white LEDs, *Inorg. Chem.*, 2019, **48**, 4412–4419.

30 Y. Heeyeon, K. Yoshihiro, Y. Hee Chang, J. P. Sang, H. O. Ji and R. D. Young, Sn–P–F containing glass matrix for the fabrication of phosphor-in-glass for use in high power LEDs, *RSC Adv.*, 2016, **6**, 111640–111647.

31 G. C. Adhikari, S. Thape and H. Y. Zhu, Mg^{2+}-alloyed all-inorganic halide perovskites for white light-emitting

diodes by 3D-printing method, *Adv. Opt. Mater.*, 2019, **7**, 1900916.

32 V. Castaing, A. D. Sontakke, A. J. Fernandez-Carrion, N. Touati, L. Binet, M. Allix, D. Gourier and B. Viana, Persistent luminescence of ZnGa$_2$O$_4$:Cr^{3+} transparent glass ceramics: effects of excitation wavelength and excitation power, *Eur. J. Inorg. Chem.*, 2017, **44**, 5114–5120.

33 P. F. Li, M. Y. Peng, L. Wondraczek, Y. Q. Zhao and B. Viana, Red to near infrared ultralong lasting luminescence from Mn^{2+}-doped sodium gallium aluminum germanate glasses and (Al,Ga)-albite glass-ceramics, *J. Mater. Chem. C*, 2015, **3**, 3406.

34 T. Hu, H. Lin, J. Xu, B. Wang, J. M. Wang and Y. S. Wang, Color-tunable persistent luminescence in oxyfluoride glass and glass ceramic containing Mn^{2+}:α-Zn$_2$SiO$_4$ nanocrystals, *J. Mater. Chem. C*, 2017, **5**, 1479–1487.